NANO-MECHANICAL CHARACTERIZATION OF DISCONTINUOUSLY REINFORCED TITANIUM COMPOSITE

Yoshihisa Tanaka*, Jenn-Ming Yang, Takahito Ohmura* Yu-Fu Liu***, Yutaka Kagawa*, ***

* National Institute for Materials Science,
** University of California, Los Angeles
***The University of Tokyo**

Keywords: *nano-mechanical characterization, in-situ AFM observation, nanoindentation*

Abstract

Microstructure-related local deformation and fracture behavior was evaluated using in-situ atomic force microscope (AFM) observation and nanoindentation techniques for a discontinuously-reinforced Ti-6Al-4V composite. . The material used was a TiB whisker and TiC particle reinforced Ti-6Al-4V composite. The evolution of surface roughness and slip band spacing was quantified as a function of applied strain. The microstructural damage during tensile loading was also studied. The results from in-situ AFM observation during tensile loading clearly show that the formation of slip bands in the Ti-6Al-4V matrix was clearly observed at the applied strain above 1.3%. The amount of slip bands and surface roughness increase with increasing applied strain. The rupture of TiC particle and multiple cracking of TiB whiskers were observed at the applied strain above 1.9%. The interaction of slip bands with the reinforcements, and mechanisms of deformation and fracture of the composite were elucidated.

The hardness and the modulus of the TiB whisker and the matrix phase were evaluated quantitatively by nanoindentation. The load-penetration curve of the TiB whisker at the peak load of 2000 mN clearly shows a significant pop-in event at approximately 1270 mN. The measured pop-in load was found to vary between 1200 and 1800 mN.

1 Introduction

Discontinuously reinforced titanium composites with high strength, high stiffness and low density are promising materials for aerospace and automotive applications. Titanium monoboride (TiB) is attractive because of its high hardness and stiffness, its low density and chemical stability with titanium matrix. Furthermore, during powder-metallurgy processing, TiB reinforcement can be synthesized in-situ within titanium alloy matrix by the solution of TiB_2 particles and subsequent re-presentation of TiB whisker [1-3]. Understanding the micromechanisms of deformation and fracture is necessary to consider the composite practical applications. It is very widely recognized that the mechanical properties of the composite materials are strongly affected by local events such as voids nucleation at the reinforcement/matrix interface, fracture of the reinforcement, initiation and propagation of matrix shear slip bands and the linkage of these local damage [4]. The efficiency of the stress transfer from the matrix to short fiber reinforcements such as whisker or particle plays an important role in determining the mechanical performance. Gorsse and Miracle [5] showed that the strength and ductility of TiB whisker-reinforced titanium composite (TiB/Ti) associated with the microstructure and the reinforcement distribution, and damage occurred from large-sized or clustered whiskers at low strain levels and propagated through the whiskers rather than at the reinforcement/matrix interface. Soboyejo et al. [6] showed that predominant fatigue crack growth mechanism of TiB/Ti composite was the onset of transverse cracking across the TiB whiskers and the TiB whisker bridging which operated behind the crack tip.

To understand the fracture behavior, in-situ scanning electron microscope (SEM) observations have been carried out for TiB whisker reinforced titanium alloy matrix composites (TiBw/Ti) [7,8]. Although in-situ SEM observation technique have given some very interesting results, there are no reports regarding the effect of surface nano deformation on the damage and fracture processes in discontinuously reinforced titanium composites is not fully understood.

The atomic force microscope (AFM) is a powerful tool to analyze the characteristics of three-dimensional surface features with nanometer dimensions. Using in-situ AFM instead of in-situ SEM observation has several advantages: (i) both in-plane and out-of-plain deformation can be evaluate simultaneously at the nanoscale resolution, (ii) the experiments are carried out in ambient condition without vacuum, (iii) the electrical conductivity for materials is not necessary. AFM has been used to observe slip bands produced by static and fatigue loading; and to study the mechanisms of fatigue crack initiation and damage evolution in several different metallic alloys including aluminum, copper and stainless steels [9-12].

On the other hand, it is now widely recognized that features in nanoindentation load-penetration curves can provide valuable insights into the response of materials during deformation. For example, significant features in the load-penetration curve can be associated with microstructural events including cracking, initiation and propagation of dislocations [13, 14]. However, there is no experimental investigation on damage nucleation in the reinforcements of the TiB/Ti composites.

In the present study, direct observation of nano-scale deformation in discontinuously reinforced Ti composite during tensile loading was conducted by an in-situ AFM observation. The nano-mechanical response of the TiB whisker was investigated using nano-indentation.

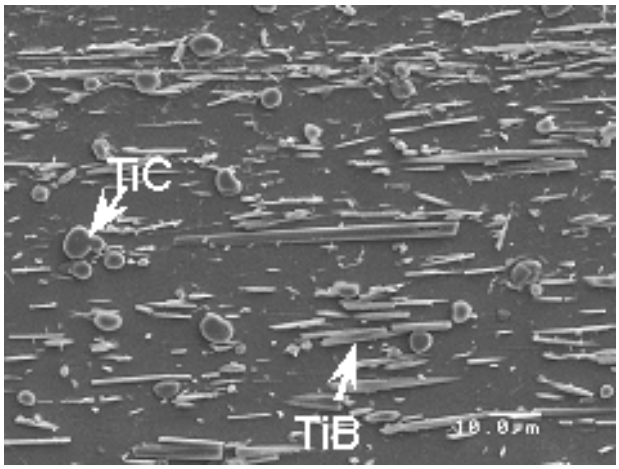

Fig.1 Microstructure of the composite.

2 Experimental Procedure

2.1 Composite Material

The composite material used in this study was an in-situ TiC and TiB reinforced Ti-6Al-4V composite produced by Crucible Research LLC (Pittsburgh, PA). The composition of the alloy was Ti-6Al-4V-1.1B-0.8C (all in weight percent). The pre-alloyed powder reinforced with TiB and TiC was produced by adding boron and carbon to a titanium alloy melt via induction skull melting followed by inert-gas atomization. The atomized powder was consolidated using hot isostatic pressing (HIPing) at 1000 °C followed by extrusion at 1095 °C into a plate. A typical example of the polished extruded section of the composite is shown in Figure 1. The sample was cut directly from the extruded bar and was polished and etched with a solution of water, nitric acid, and hydrofluoric acid in proportions of 85:10:5. The microstructure consists of TiB whiskers with diameters ranging from 0.2 to 3 μm (the average size: ≈1.6 μm), and the equiaxed TiC particles with diameters ranging from 3-5 μm. The effect of extrusion in aligning the TiB whisker in the direction of extrusion is apparent. The volume fraction of TiB whisker and TiC particle in the composite is close to 5.5 and 4 %, respectively. The particles presented irregular shapes, with sharp corners, and were usually oriented with their longer axis in the extruded direction.

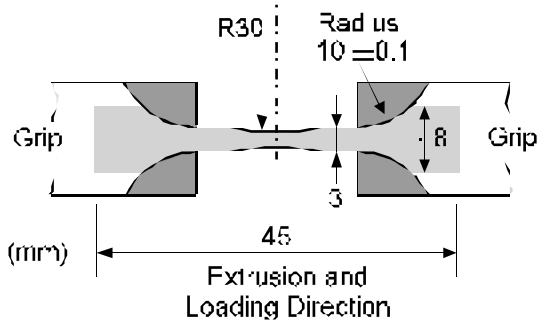

Figure 2 Shape and dimensions used for in-situ observation.

2.2 In-situ AFM Observation

A special loading device was built to fit in the AFM (AutoProbe M5, Nihon Veeco Corp.). The maximum loading capacity of the device is 2KN. The load increment was controlled precisely by a stepping motor. The specimens for in-situ tensile tests were prepared using electrical discharge machining method with loading parallel to the extruded direction. The central parts of the specimens had a dog-bone shape with a width of 2.5 mm and a thickness of 1.2 mm as shown in Figure 2. To allow a direct observation of damage progression, one surface of the specimen was progressively polished with diamond paste up to 0.25 mm, and was finally polished with a solution of MASTERMET (Buehler, Ltd.) which has a SiO_2 particle size of 60 nm in an aqueous base (10 pH), hydrogen peroxide, and ammonia water of 92:4:4.

A strain gauge was also mounted on the back side of the specimen to record the elongation during tensile loading. The test was conducted at a cross-head speed of 0.01 mm/min. The loading was stopped after a predetermined amount of strain increment to allow AFM observation of surface deformation as indicated by arrows in the Figure 3 with a stress-strain curve. The tip was scanned across a small surface area to sample the surface topography with a non-contact mode at a frequency of 320 KHz, and a resolution of 512×512 pixels. To minimize creep deformation in air during in-situ AFM observation, the specimen was unloaded to the elastic deformation region (around 500 MPa). The

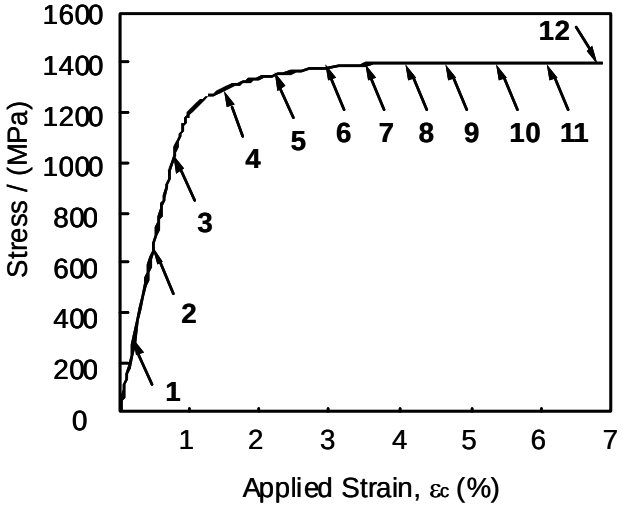

Figure 3 A typical stress-strain curve of the in-situ TiB and TiC reinforced Ti-6Al-4V composite.

surface roughness profiles and surface average roughness amplitude, Ra, were analyzed by built-in software.

The surface average roughness amplitude, R_a, was defined as:

$$R_a = \frac{1}{L_x L_y}\int_0^{L_x}\int_0^{L_y}\left|f(x,y)\right|dxdy, \quad (1)$$

where f(x, y) is the surface function of the roughness profile relative to the center plane and Lx and Ly are the measured lengths for loading and rectangular to the loading direction, respectively. The optical microscope equipped with a CCD camera was used to find the appropriate mark on the center of the specimen.

The optical microscope equipped with a CCD camera was used to find the appropriate mark on the center of the specimen. The fracture surface was examined by a scanning electron microscope.

2.2 Nano-Mechanical Properties

Nanoindentation experiments were carried out using a Hysitron, Inc. Triboindenter. A Berkovich indenter was employed, and the tip truncation was calibrated using a reference specimen of fused silica. Analyses for the tip calibration and the calculation of nanohardness, Hn, were conducted using the Oliver and Pharr method [15]. The reduced modulus, E_r, was also calculated by an analysis of an unloading curve, and is expressed as

$$\frac{1}{E_r} = \frac{1-\nu_s^{\,2}}{E_s} + \frac{1-\nu_{ndi}^{\,2}}{E_{ndi}}, \quad (2)$$

where E_s and ν_s are Young's modulus and Poisson's ratio for the specimen and E_{ind} and ν_{ind} are the same parameters for the indenter. The probed sites and the shape of the indent marks on the specimen surface were confirmed before and after the indentation measurements with the scanning probe microscope (SPM) capabilities of a Triboindenter. The obtained SPM images are represented not as a topographic image but as a gradient image in this study because the indent marks can be seen more clearly in the gradient images.

3 Results and Discussion

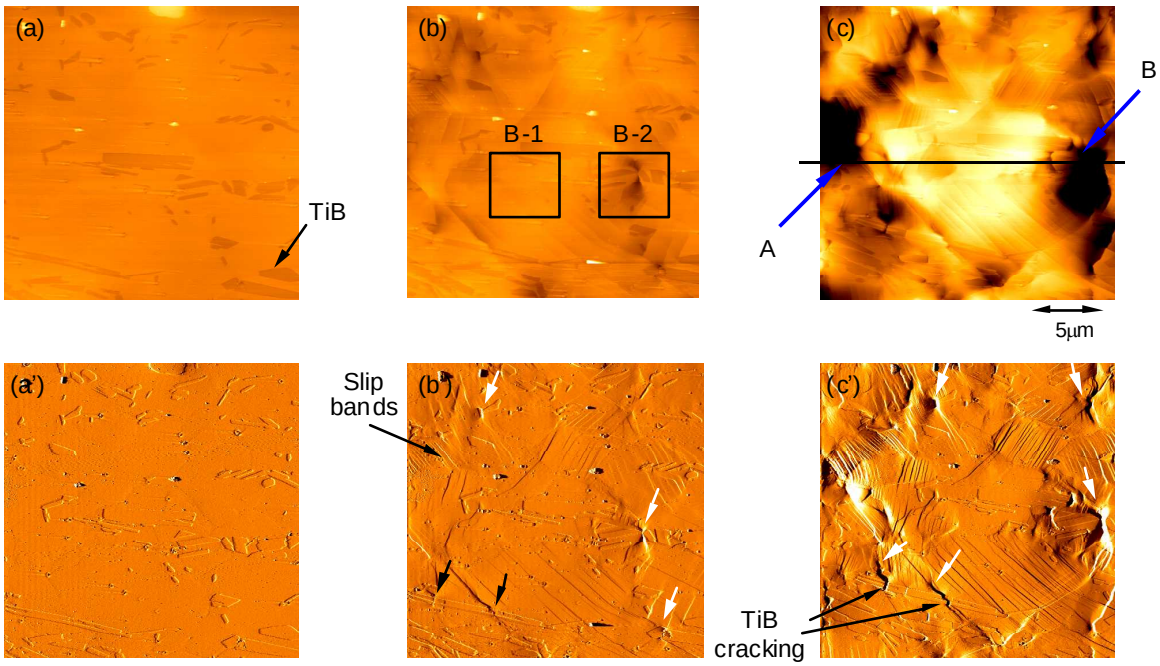

Figure 4 The evolution of surface morphology and the roughness height derivative image of the composite reinforced with TiB whisker observed under a AFM at three different strain levels: (a) and (a') ε_c = 0.8%, (b) and (b') ε_c = 1.9%, (c) and (c') ε_c = 4.7%.

3.1 Nano-Scale Surface Damage Evolution

The evolution of surface morphology with the roughness height derivative image observed under a AFM at three different strain levels, ε_c = 0.8, 1.9 and 4.7 % are shown in Figures 4. In the surface morphology image, the reinforcement on the surface can be clearly seen before straining, but the details of damage evolution such as cracking of whisker and matrix slip bands with increasing the strain is obscured due to the presence of large surface roughness. The roughness height derivative image can resolve the details of such damage events, as indicated by (a'), (b') and (c') in the figures, respectively. no slip band was observed at a strain level of 0.8 %, since it is still within the elastic deformation regime. As the applied strain was increased to beyond the elastic range, slip bands were observed at a strain level of 1.3%. Cracking of TiB whisker (as indicated by black arrows in

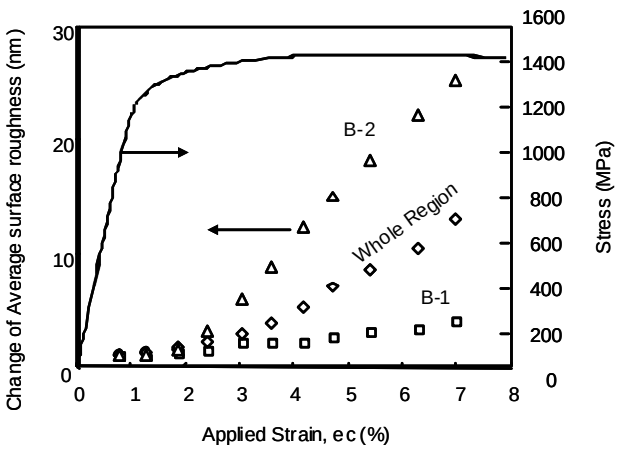

Figure 5 Change of surface roughness at the different regions as a function of applied strain with stress-strain curve of the composite.

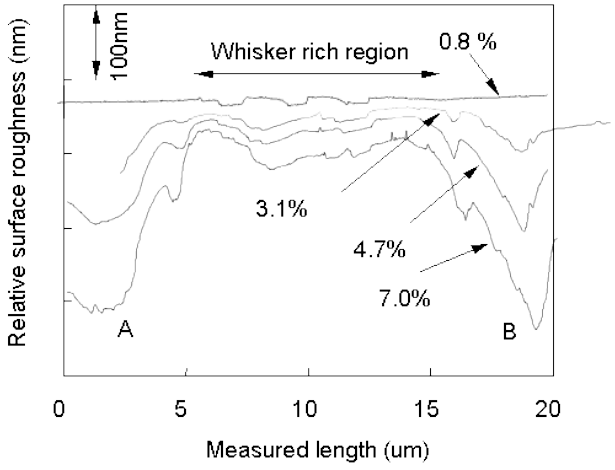

Figure 6 Relative surface roughness profiles of a line in Figure 4(c) based on various step of different applied strain.

figures) were also observed at about the same strain level. When the applied strain was increased to 1.9%, localized deformation at the whisker end (as indicated by white arrows in figures) and the formation of more slip bands were clearly observed in the roughness height derivative images (figure 4(b')). As the applied strain was further increased to 4.7%, a significant amount of slip bands were observed as shown in Figures 4(c). Decreasing slip band spacing with increasing plastic deformation in the matrix suggests that the cumulative local shear strain in the slip bands is strongly related to local plastic strain. Furthermore, the crack opening of the ruptured TiB whisker, and the localized deformation areas near the whisker ends were found to increase with increasing strain (figure 5(c')).

The change of average surface roughness defined as $R_a(\varepsilon_c)/R_a(\varepsilon_c=0)$ versus applied strain in the composite at three different regions is plotted in Figure 5. The average surface roughness of two different 5×5 mm^2 regions with different microstructural features as boxed in Figure 4(b) and the whole region are plotted. Evidently, the average surface roughness increased as the applied strain in the composite increased for all regions. Obviously, plastic deformation through the formation of slip bands would mainly roughen the surface [9]. The change of surface roughness in regions of B-1 and B-2 are significant different. The surface roughness in region B-2 increased rapidly after straining beyond 1.8% due to severe localized deformation at the end of several TiB whiskers. On the other hand, the surface roughness in region B-1, which contains a higher volume fraction of TiB whiskers (without the presence of whisker ends), was not increased with increasing strain. Figure 6 shows the surface roughness profiles of a line in Figure 4(c) based on various step of different applied strain. It is clearly shown that the localized deformation at the point of A and B near the whisker ends were found to increase with increasing applied strain. These differences suggest that the localized surface plastic deformation is significantly affected by local events such microstructural inhomogeneity and anisotropy, size and distribution of the reinforcements, reinforcement cracking, slip bands formation and interfacial shear strength.

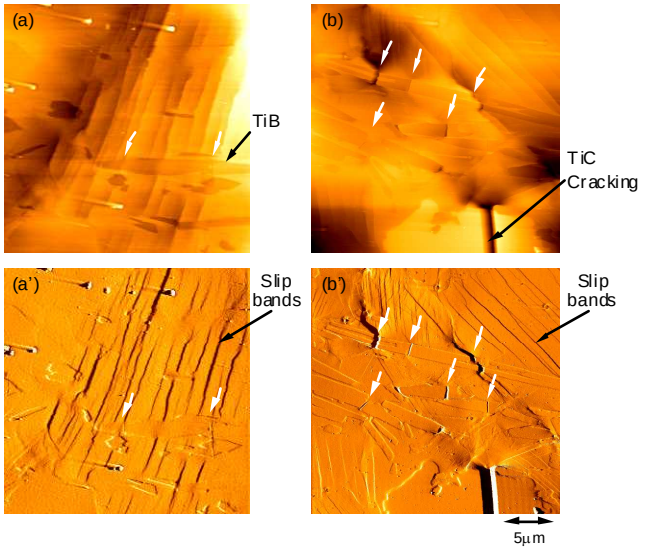

Figure 7 Morphology of slip bands and its interaction with TiB whisker: (a) and (a') contains TiB only, (b) and (b') contains both TiB and TiC.

Figure 7 shows the interaction between slip bands and TiB whisker. The multiple fracture of TiB

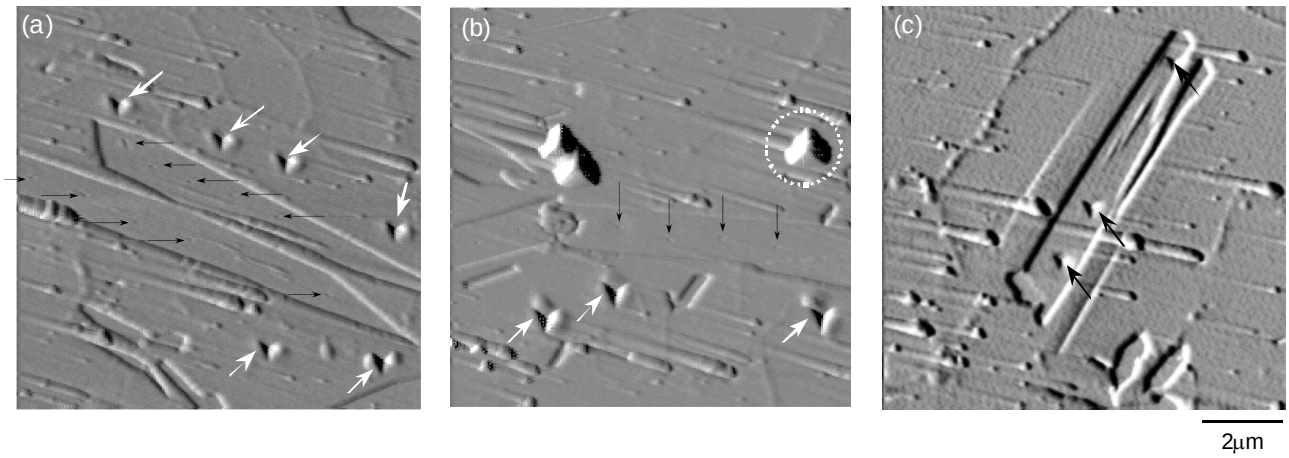

Figure 8 Scanning prove microscopy images of the composite contained with TiB whisker after nanoindentation: (a) the peak load, P=500 μN, (b) P=1000 μN, and (c) P=2000 μN. (The triangular indents marked on the TiB whisker and the matrix indicates as black and white arrows, respectively.)

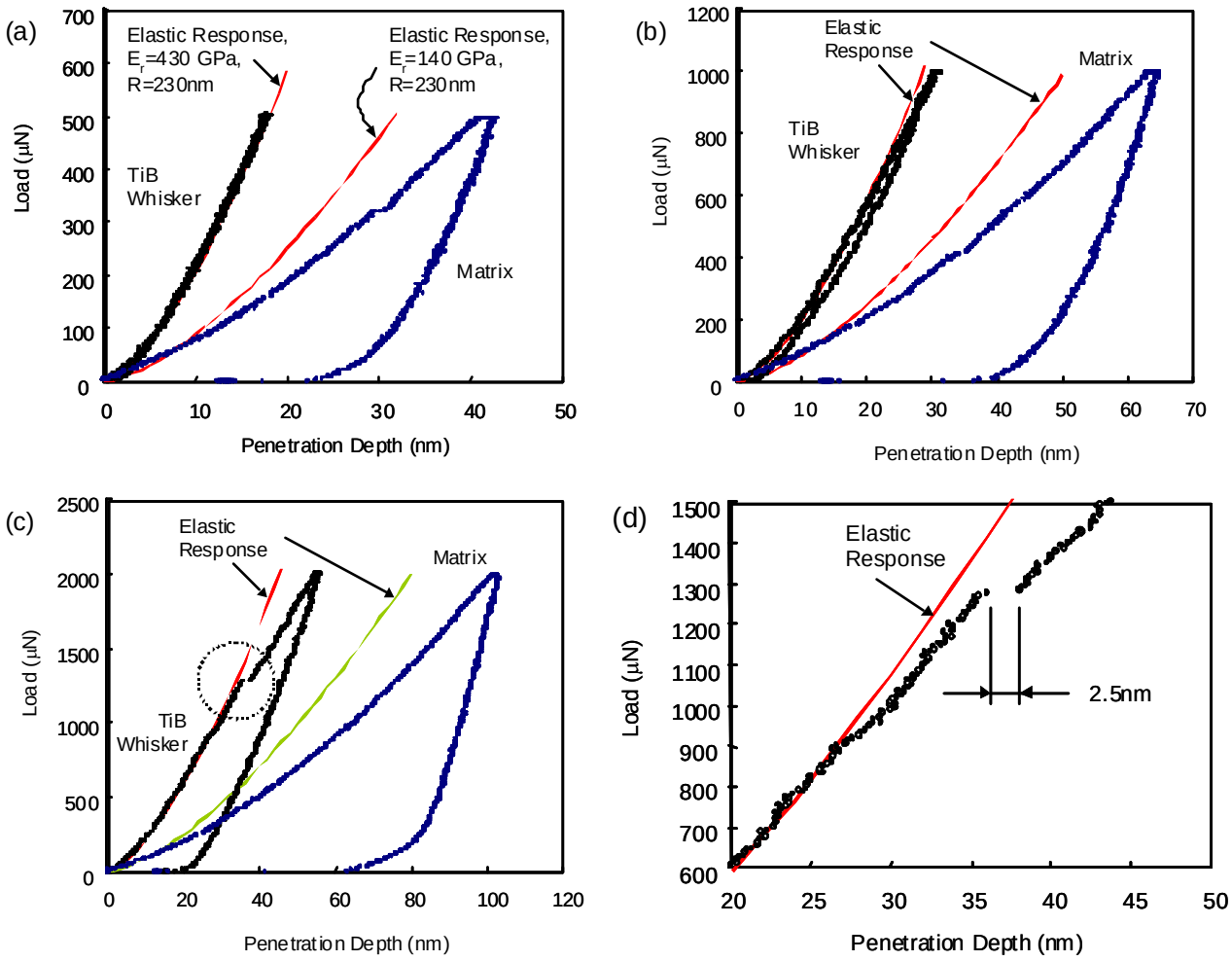

Figure 9 Load-penetration curves of TiB whisker and the matrix: (a) the peak load of P=500 μN, (b) P=1000 μN, (c) P=2000 μN, and (d) detail of the loading curve in a circle region of (c). The elastic portion of the load-penetration curves of both the TiB whisker and the matrix calculated from Eq. (3) are shown in Figure (a), (b) and (c).

whisker is clearly observed near the slip bands as indicated by white arrows in the figure. It appears that when a shear slip band intersects a TiB whisker, the stress concentration due to dislocation pile-up may cause the shear and/or tensile failure of the whisker. It has been showed that the fracture of discontinuous fiber by slip bands plays a significant role in the damage evolution process of the composite.

3.2 Nano-Mechanical Properties

The continuous deformation characteristics of the TiB whisker and titanium matrix was investigated using a nanoindentation technique. For this purpose, systematic nanoindentation experiments were conducted on both the TiB whisker and the matrix. Special attention has been focused on the effect of the peak load on the nanoindentation response in order to account for any peak load dependence on the elastic-plastic behavior for both the whisker and the matrix.

Figure 8(a), (b) and (c) shows the SPM images contained with TiB whisker after indentation measurement at the peak load of 500, 1000 and 2000 μN, respectively. The micrographs include several triangular indents marked on the whisker and the matrix as some indents indicated by black and white arrows. It is difficult to observe several indents marks on the whisker at the peak load of 500 and

1000 μN, but is clearly observed at the peak load of 2000 μN. The penetration depth of TiB whisker is much shallower than that of the matrix at the same peak load, for example the residual indentation depth on the whiskers at the peak load of 500, 1000 and 2000 μN are 0.8, 2.5 and 18 nm. The SPM images show many triangular pyramids that are indicated by circle as in Figure 8(b). This is the so called "convolution effect" on SPM imaging. When a probe scans a convexity with an aspect ratio that is lower than that of the probe, the image shows the geometry of the probe rather than the convexity itself.

Typical Load-penetration curves of TiB whisker and the matrix at the peak load of 500, 1000 and 2000 μN are shown in Figure 9(a), (b) and (c), respectively. A diamond Berkovich pyramid indenter with a tip radius R=230 nm was used, which was estimated for the present device shown in previous work [16]. The penetration depth h_t=0.09R estimates about 21 nm. Therefore, the elastic portion of the load-penetration curve for a spherical indenter [13] is calculated as

$$P = \frac{4}{3} E^* * h^{3/2} * R^{1/2}. \qquad (3)$$

Plotted along with the experimental curves for the spherical tip is the theoretically predicted elastic indentation response from equation (3) for TiB whisker and the matrix. The value of E_r used for the theoretical curves was $E_{r,TiB}$=323 GPa and $E_{r,Ti}$=138 GPa, as calculated from equation (2), using the values $E_{s,TiB}$=450 GPa [5] and $\nu_{s,TiB}$=0.14 for the TiB whisker, and $E_{s,Ti}$=140 GPa [1] and $\nu_{s,Ti}$=0.32 for the Ti-6Al-4V matrix, and E_{ind}=1140 GPa and ν_{ind}=0.07 for the diamond indenter (ISO 14577 – 2002 [17]), respectively. The Poisson's ratio of TiB whisker, $\nu_{s,TiB}$, is not available in the literature. For the present calculation, it is assumed that $\nu_{s,TiB} = \nu_{s,TiB2}$. The value of $\nu_{s,TiB2}$ was adopted in the literature [18]. It can be seen that the load-penetration depth curves for TiB whisker at three different peak loads below $\approx$ 800 μN are in reasonable agreement with the predicted sharp indenter elastic response.

The load-penetration depth curve of TiB whisker at the peak load of 2000 μN clearly shows a significant pop-in event at approximately 1270 μN in load, as indicated by a circle in Figure 9(c). The measured pop-in load was found to vary between 1200 and 1800 μN, and the pop-in extension is approximately 2.5 nm, as defined in Figure 9(d), showing a specific deformation behavior.

On the other hand, the matrix yield point is observed at the load from 100 to 200 μN. The calculated elastic depth of penetration is approximately 15 nm and the elastic-plastic response occurs after the yield point.

The pop-in on the load-penetration curve is considered to correspond to the change of deformation mode from elastic to elastic-plastic response, as described in previous papers [13, 19-21]. It may be associated with several microstructural damage including cracking, interface debonding and the nucleation and propagation of dislocations. Further microstructural analysis using focus ion beam/TEM analysis is being conducted to better understand the damage nucleation mechanisms for TiB whisker.

Calculated nanohardness, H_n, and reduced modulus, E_r, obtainded from nanoindentation measurement are summarized in Table I. In nanoindentation experiment, the maximum penetration depth, h_{max}, must obey to the length scale separability condition of $h_{max} \leq D/10$. D represents the characteristic size of the heterogeneity within TiB whiskers. SEM images of the composite (see Figure 1) suggest that the average size of 1.6 μm is characteristic of TiB whiskers. An appropriate penetration depth allows access to the TiB whiskers by nanoindentation is $h_{max} \leq 160$ nm. The experimental results show that the reduced modulus and the nanohardness decrease with increasing the peak load, despite the maximum penetration depth satisfied the condition of h_{max}. It is considered that the decrease of the modulus and the nanohardness occur due to the substrate effect related to the matrix phase. On the other hand, the nanohardness and the modulus for the matrix phase is independent on the peak load.

4. References

[1] K. S. Ravi Chandran, K. B. Panda and S. S. Sahay, TiBw-reinforced Ti composites: processing, properties, application prospects, and research needs. JOM 56-5, pp 42-48, 2004.

[2] T. Saito, Automotive application of discontinuously reinforced TiB-Ti composites. JOM 56-5, pp 33-36, 2004.

[3] C. F. Yolton, The pre-alloyed powder metallurgy of titanium with boron and carbon additions. JOM 56-5, pp 56-59, 2004.

[4] M. Geni and M. Kikuchi, Damage analysis of aluminum matrix composite considering non-uniform

distribution of SiC particles, Acta Mater., vol.46, pp 3125-3123, 1998.

[5] Gorsse and D. B. Miracle, Mechanical properties of Ti-6Al-4V/TiB composites with randomly oriented and aligned TiB reinforcements. Acta Mater. Vol. 51, pp 2427-2442, 2003.

[6] W.O. Soboyejo, W. Shen and T.S. Srivatsan, An investigation of fatigue crack nucleation and growth in a Ti-6Al-4V/TiB in situ composite, Mech. Mater., 36, pp 141-159 2004.

[7] B.S. Li, J.L. Shang, J.J. Guo and H.Z. Fu, In-situ observation of fracture behavior of in situ TiBw/Ti composites, Mat. Sci. Eng., A383, pp 316-322, 2004.

[8] C.J. Boehlert, C.J. Cowen, S. Tamirisakandala, D.J. McEldowney and D.B. Miracle, In situ scanning electron microscopy observation of tensile deformation in a boron-modified Ti-6Al-4V alloy, Scripta Materialia, 55, pp 465-468, 2006.

[9] W. Long, L. G. Hector, H. Weiland and L. F. Wieserman, In-situ surface characterization of a binary aluminum alloy during tensile deformation. Scripta Mater, 36, pp 1339-1344, 1997.

[10] J. Man K. Obrtlik, C. Blochwitz and J. Polak, Atomic force microsopy of surface relief in individual grains of fatigued 316L austenitic stainless steel, Acta Materialia, 50, pp 3767-3780, 2002.

[11] L. Cretegny and A. Saxena: AFM characterization of the evolution of surface deformation during fatigue in polycrystalline copper. Acta Mater, 49, pp 3755-3765, 2001.

[12] M. Risbet, X. Feaugas, C. Guillemer-Neel and M. Clavel, Use of atomic force microscopy to quantify slip irreversibility in a nickel-base superalloy, Scripta Materialia, 49, pp 533-538.

[13] A. Gouldstone, H.J. Koh, K.Y. Zeng, A.E. Giannakopoulos and S. Suresh, Discrete and continuous deformation during nanoindentation of thin films, Acta Mater., 48, pp 2277-2295, 2000.

[14] T. Ohmura, K. Tsuzaki, K. Sawada and K. Kimura, Inhomogeneous nano-mechanical properties in the multi-phase microstructure of long-term aged type 316 stainless steel, J. Mater. Res. Vol. 21, No.5, pp 1229-1236, 2006.

[15] W.C. Oliver and G.M. Pharr, An improved technique for determining hardness and elastic modulus using load and displacement sensing indentation experiments, J. Mat. Res., 7, pp 1564-1583, 1992.

[16] T. Ohmura, K. Tsuzaki and F. Yin, Nanoindentation-induced deformation behavior in the vicinity of single grain boundary of interstitial-free steel, Mater. Trans. 46, pp 2026-2029, 2005.

[17] ISO 14577, Metallic Materials – Instrumented Indentation Test for Hardness and Materials Parameters, 2002.

[18] R.G. Munro, Material properties of titanium diboride Journal of Research of the National Institute of Standards and Technology, Vol. 105, pp 709-720, 2000.

[19] W.W. Gerberich, J.C. Nelson, E.T. Lilleodden, P. Anderson and T. Wyrobek, Indentatio induced dislocation nucleation: The initial yield point, Acta Mater., 44, pp 3585-3598, 1996.

[20] S. Suresh, T.G. Nieh and B.W. Choi, Nanoindentation of copper thin films on silicon substrates, Scripta Mater., 41, pp 951-957, 1999.

[21] A. Gouldstone, K.J. Koh, Van Vliet and S. Suresh, Simulation of defect nucleation in a crystal, Nature, 411, pp 656-656 , 2001.

[22] K.L. Johnson, Contact Mechanics, Cambridge University Press, Cambridge, UK, 1985.